J. Fluid Mech. (2006), *vol.* 563, *pp.* 199–222.
doi:10.1017/S0022112006001170 Printed in the United Kingdom

Vortex–wave interaction in a rotating stratified fluid: WKB simulations

By F. Y. MOULIN AND J.-B. FLÓR

LEGI, Grenoble, France

(Received 12 May 2004 and in revised form 6 February 2006)

In this paper we present ray-tracing results on the interaction of inertia–gravity waves with the velocity field of a vortex in a rotating stratified fluid. We consider rays that interact with a Rankine-type vortex with a Gaussian vertical distribution of vertical vorticity. The rays are traced, solving the WKB equations in cylindrical coordinates for vortices with different aspect ratios. The interactions are governed by the value of FrR/λ where Fr is the vortex Froude number, R its radius, and λ the incident wavelength. The Froude number is defined as $Fr = U_{max}/(NR)$ with U_{max} the maximum azimuthal velocity and N the buoyancy frequency. When $FrR/\lambda > 1$, part of the incident wave field strongly decreases in wavelength while its energy is trapped. The vortex aspect ratio, H/R, determines which part of this incident wave field is trapped, and where its energy accumulates in the vortex. Increasing values of FrR/λ are shown to be associated with a narrowing of the trapping region and an increase of the energy amplification of trapped rays. In the inviscid approximation, the infinite energy amplification predicted for unidirectional flows is retrieved in the limit $FrR/\lambda \to \infty$. When viscous damping is taken into account, the maximal amplification of the wave energy becomes a function of FrR/λ and a Reynolds number, $Re_{wave} = \sqrt{U_L^2 + U_H^2}/\nu k^2$, with U_L and U_H typical values of the shear in, respectively, the radial and vertical directions; the kinematic viscosity is ν, and the wavenumber k, for the incident waves. In a sequel paper, we compare WKB simulations with experimental results.

1. Introduction

Vortex–wave interactions play an important role in many large-scale and meso-scale geophysical flows. The transition from three- to quasi-two-dimensional turbulence owing to background rotation, stratification and flow geometry in large-scale geophysical flows involves the organization into large- and meso-scale vortices, while waves are continuously generated by geostrophic adjustment processes. The associated wave–vortex interactions are a subject of recent study.

Next to vortical modes, that evolve on an advection time scale R/U with U and R, respectively, the horizontal velocity and vortex length scale, relatively fast internal waves evolve on a time scale based on the buoyancy frequency N. Wave–vortex interactions can be considered as a function of a horizontal Froude number Fr, which compares these two different time scales. For a non-rotating fluid and in the limit of very small Fr, Lelong & Riley (1991) have predicted weakly nonlinear interactions between waves and vortical modes. Galmiche, Thual & Bonneton (2000) showed that the mean oscillating flow produced during interacting internal gravity waves, may lead to wave-breaking by retrograde interaction and generate a non-zero potential vorticity field.

Critical layers and wave-breaking in parallel shear flows have been explored experimentally, numerically and theoretically over the past three decades in view of their fundamental role in momentum transport and mixing properties (see e.g. Booker & Bretherton 1967; Ivanov & Morozov 1974; Olbers 1980; Koop 1981; Badulin, Shrira & Tsimring 1984; Badulin & Shrira 1993; and references in Staquet & Sommeria 2002). The energy of the incident wave packet accumulates as its wavelength decreases to zero. In critical layers of jets or parallel shear flows, waves are reflected, absorbed or break, leading to instabilities and turbulence (see e.g. Dörnbrack 1998; Staquet & Huerre 2002). Edwards & Staquet (2005) investigated the interaction of a wave packet with a baroclinic jet, showing a succession of reflections within the jet. Presumably because of their specific choice of initial conditions they, however, did not find evidence of wave-breaking. The effects of nonlinearities for the interaction with a critical layer have been addressed for a vertical shear (see Jones 1968; Acheson 1976; van Duin & Kelder 1982) or a horizontal shear (see Öllers 2003). These studies show that overreflection occurs only when the flow is intrinsically unstable for Kelvin–Helmoltz and inertial instabilities, respectively. In this paper, we address the question of what happens with inertia–gravity waves in a vortex, of which the shear flow is curved and finite in space.

Interactions of externally generated waves with a vortex have been investigated for a number of cases. In an experimental study related to the present investigation (Moulin & Flór 2005), we have shown that wave-breaking in the periphery of a vortex leads to a deposit of anti-cyclonic vorticity. Bühler & McIntyre (2003) have studied the effect of surface waves on a singular vortex with outer potential flow in the limit of a small Froude number, i.e. with fast phase speeds compared to a slow vortex motion. They show that the vortex core is advected by horizontally refracted waves. In the presence of standing waves, dipolar vortices in a pycnocline were found to oscillate in translation velocity due to both the wave-induced stretching and squeezing of vertical vortex tubes within the dipolar structure, and the continuous change in the mutual distance of the vortices (see Flór, Fernando & Van Heijst 1994).

The interaction of planar waves with the velocity field of a monopolar vortex can be characterized by the ratio of the phase speeds of the vortex and wave given by R/T_v, and Λ/T_w, respectively, with Λ the wavelength, and T_v and T_w the vortex and wave periods. When the phase speed of the wave is larger than the maximum velocity in the vortex, $\Lambda/T_w > R/T_v$, no wave-breaking can be expected. In contrast, when $\Lambda/T_w < R/T_v$ the waves are constrained by the Doppler effect and either reflect, break or are absorbed. These effects also depend on the curvature of the flow field in the vortex, as becomes clear when introducing an interaction length $l = \Lambda T_v/T_w$ of the wave with the vortex. The interaction is again small when $l/R > 1$, corresponding to the first case, whereas the interaction is strong for values $l/R < 1$. In the present paper, we focus on interactions of planar waves with an individual vortex for $l/R < 1$ and include effects of flow curvature.

Since we apply the WKB approach, we will briefly introduce its basic theory for wave interactions with a parallel shear flow. The WKB theory applies mainly to flows with low Rossby and Froude numbers. It assumes that the phase of the wave evolves on time and space scales shorter than the scales associated with the changes in amplitude. Local values of the wavenumber and the frequency of the wave can be deduced from the spatial and temporal derivatives of the phase function. The energy propagates along rays of which the trajectories are inferred from the local values of the group velocity and the background flow. The time-dependence of the wave field is given by its absolute frequency, ω_{abs}, corresponding to the wave frequency before

the interaction. During the interaction, this time-dependence is conserved, and the intrinsic frequency of the wave, ω_o, defined as its frequency in a referential moving with the local mean flow velocity, $\boldsymbol{U}$, is inferred from the Doppler shifting relationship

$$\omega_{abs} = \omega_o + \boldsymbol{k}\cdot\boldsymbol{U}, \tag{1.1}$$

where $\boldsymbol{k}$ is the local wavenumber. The wave number component parallel to the flow is conserved according to WKB theory. The wave intrinsic frequency, ω_o, of planar incident waves depends, according to the Doppler relationship, only on the spatial position $\boldsymbol{r}$. The flow is divided into regions where waves can propagate $|\omega_o| \in [f, N]$, with f the Coriolis parameter and N the buoyancy frequency, or are arrested, $|\omega_o| < f$ or $|\omega_o| > N$. The limits of these regions are known as reflection or critical layers. The WKB theory remains valid near reflection layers, whereas near critical layers the energy tends to infinity, indicating the trapping of waves. Near critical layers, the linear approximation becomes singular.

For waves in a stratified shear flow, Koop (1981) compared analytical solutions of the WKB equations with experiments and showed that the intrinsic frequency goes to N near a reflection layer, whereas it goes to 0 near a critical layer. Because of viscous damping, wave-breaking could not be observed. Olbers (1980) considered a geostrophic jet and showed that the components of the wave number parallel to the iso-velocity surfaces are conserved. Depending on their propagation direction, the waves are either trapped in a 'valve'-like critical layer or escape. In the limit of a purely horizontal shear flow, this critical layer merges with the layer $\omega_o = 0$. Waves propagating against the flow are trapped near a critical layer $\omega_o = N$, in agreement with predictions by WKB theory, and break through a buoyancy-induced instability. In a more general context, the trapping and reflection of the waves are still represented by the WKB theory (e.g. Badulin & Shrira 1993).

In § 2, we derive the equations of the WKB approximation for axisymmetric background flows in cylindrical coordinates, and apply them to a Rankine-type vortex. Ray-tracing results for the inviscid interaction of inertia–gravity waves with an incident planar wave field are presented in § 3. To estimate the effects of flow curvature and viscous damping, the results obtained for a simplified flow-model are discussed in § 4, and conclusions and perspectives are presented in § 5.

2. WKB theory for vortex-like flows

2.1. *Governing equations*

In this subsection we derive the WKB theory for waves in the velocity field of a vortex. The Boussinesq equations for a flow in a rotating and linearly stratified fluid of mean density ρ_o, buoyancy frequency N_o and Coriolis parameter f are written in the form

$$\left(\frac{\partial \boldsymbol{u}}{\partial t} + (\boldsymbol{u}\cdot\nabla)\boldsymbol{u}\right) = -f\boldsymbol{e}_z \times \boldsymbol{u} - \frac{\nabla P}{\rho_o} + \frac{\rho}{\rho_o}\boldsymbol{g}, \tag{2.1}$$

$$\nabla\cdot\boldsymbol{u} = 0, \tag{2.2}$$

$$\left(\frac{\partial \rho}{\partial t} + (\boldsymbol{u}\cdot\nabla)\rho\right) - w\frac{\rho_o}{g}N_o^2 = 0, \tag{2.3}$$

where $\boldsymbol{u}$ is the flow velocity field, w its vertical component, ρ and P the density and pressure perturbations associated with the flow. N_o is derived from the vertical distribution of density $\rho_s(z)$ in the fluid at rest, $N_o = \sqrt{(-g/\rho_o)(\partial\rho_s/\partial z)}$.

We decompose the velocity field into a stationary vortex field and a wave field. The vortex has azimuthal velocity U with perturbation pressure and density field ρ_v and P_v, respectively; the wave field has velocity components $\tilde{u}$, $\tilde{v}$ and $\tilde{w}$ with density and pressure perturbation $\tilde{\rho}$ and $\tilde{p}$. Introducing the perturbations $\rho = \rho_v + \tilde{\rho}$, $\boldsymbol{u} = \tilde{\boldsymbol{u}} + U\boldsymbol{e}_\theta$ and $p = P_v + \tilde{p}$ in equation (2.3) yields two sets of equations, of which one represents the vortex motion, and the other represents the wave motion.

The vortex velocity-field is prescribed by

$$-\frac{U^2}{r} = fU - \frac{1}{\rho_o}\frac{\partial P_v}{\partial r}, \tag{2.4}$$

$$0 = -\frac{1}{\rho_o}\frac{\partial P_v}{\partial z} - \frac{\rho_v}{\rho_o}g. \tag{2.5}$$

After linearization, the equations for the wave motion read

$$\frac{\partial \tilde{u}}{\partial t} + \frac{U}{r}\frac{\partial \tilde{u}}{\partial \theta} = \left(f + \frac{2U}{r}\right)\tilde{v} - \frac{1}{\rho_o}\frac{\partial \tilde{p}}{\partial r}, \tag{2.6}$$

$$\frac{\partial \tilde{v}}{\partial t} + \frac{U}{r}\frac{\partial \tilde{v}}{\partial \theta} = -\left(f + \frac{U}{r} + \frac{\partial U}{\partial r}\right)\tilde{u} - \left(\frac{\partial U}{\partial z}\right)\tilde{w} - \frac{1}{\rho_o r}\frac{\partial \tilde{p}}{\partial \theta}, \tag{2.7}$$

$$\frac{\partial \tilde{w}}{\partial t} + \frac{U}{r}\frac{\partial \tilde{w}}{\partial \theta} = -\frac{1}{\rho_o}\frac{\partial \tilde{p}}{\partial z} - \frac{\tilde{\rho}}{\rho_o}g, \tag{2.8}$$

$$\nabla \cdot \tilde{\boldsymbol{u}} = 0, \tag{2.9}$$

$$\frac{\partial \tilde{\rho}}{\partial t} + \frac{U}{r}\frac{\partial \tilde{\rho}}{\partial \theta} = \left(\frac{\rho_o}{g}N_o^2\right)\tilde{w} + \left(\frac{\partial \rho_v}{\partial z}\right)\tilde{w} + \left(\frac{\partial \rho_v}{\partial r}\right)\tilde{u}. \tag{2.10}$$

According to the WKB approximation, the terms that represent the vortex velocity field on the right-hand side of equations (2.6)–(2.10) are neglected. The interaction of the waves with the vortex velocity-field reduces then to a Doppler shift in wave frequency, represented by the operators $(U/r)(\partial/\partial\theta)$. When replacing the absolute frequency of the wave by its intrinsic frequency, i.e. in a referential frame moving locally with the flow velocity, the eigenvalue problem for the wave frequency reduces to that of a freely propagating wave.

Scaling with the Coriolis parameter f and the buoyancy frequency N_o shows that in the limit of low vortex Rossby and Froude number, the vortex-related terms on the right-hand side of equations (2.6)–(2.10) are negligible. In contrast, for large values of the vortex Rossby number and Froude number, these right-hand side terms become important, leading to possible inertial and/or Kelvin–Helmholtz instability; the Rayleigh function $(f + U/r + \partial U/\partial r)(f + 2U/r)$ may become negative locally whereas the Richardson number $(\partial U/\partial z)^2/N_o^2$ may exhibit values smaller than 1/4.

For moderate vortex Rossby numbers ($0.1 < Ro < O(1)$), the vortex related terms on the right-hand sides of (2.6)–(2.10) remain negligible in the vortex periphery. However, near the vortex centre these terms are significant and the WKB theory becomes doubtful. From the dispersion relation it can be shown that the forbidden region for rays, defined below (§ 3), covers the vortex core. Therefore, trapped rays almost never penetrate inside the vortex core, but propagate in the vortex periphery where we can apply ray theory. This justifies the use of the WKB approximation to investigate the interaction of rays with moderate vortices.

2.2. *Basic equations of the ray theory*

The WKB theory, or ray theory, is reviewed in many textbooks in a general context (see e.g. Leblond & Mysak 1978; Lighthill 1978), and is based on the asymptotic

expansion in a small-parameter defined by the wavelength and the typical length scale of the background flow.

Here, we apply the WKB theory to a monochromatic wave field of which the time-dependence is given by its absolute frequency, ω_{abs}. The intrinsic frequency of the wave, ω_o, which is defined with respect to a referential moving with the local mean flow velocity $\boldsymbol{U}$, is inferred from the Doppler shifting relationship (1.1) and is linked to the local components of the wavenumber k_x, k_y and k_z by the dispersion relation

$$\omega_o = \sqrt{\frac{k_h^2 N^2 + k_z^2 f^2}{k_h^2 + k_z^2}}. \tag{2.11}$$

The wave field is described by the three components of the velocity $\tilde{u}$, $\tilde{v}$, $\tilde{w}$, the pressure $\tilde{p}$ and the buoyancy $\tilde{b} = -(g/\rho_o)\tilde{\rho}$, where $\tilde{\rho}$ is the density perturbation. These different components of the wave field fulfil the polarization relations

$$\begin{bmatrix} \tilde{u} \\ \tilde{v} \\ \tilde{w} \\ \tilde{b} \\ \dfrac{\tilde{P}}{\rho_0} \end{bmatrix} = A \begin{bmatrix} \omega_0 k_x + \mathrm{i} f k_y \\ \omega_0 k_y - \mathrm{i} f k_x \\ -\dfrac{\omega_0^2 - f^2}{N^2 - \omega_0^2} \omega_0 k_z \\ \mathrm{i} N^2 \dfrac{\omega_0^2 - f^2}{N^2 - \omega_0^2} k_z \\ \omega_0^2 - f^2 \end{bmatrix} \exp \mathrm{i} (\boldsymbol{k} \cdot \boldsymbol{r} - \omega_{abs} t + \phi), \tag{2.12}$$

where A and ϕ are, respectively, an amplification factor and a phase shift which evolve on time and spatial scales larger than for the wave phase $(\boldsymbol{k} \cdot \boldsymbol{r} - \omega_{abs} t)$ itself. Here, N represents the buoyancy frequency corrected for the deflection of the isopycnals due to the vortex velocity field and is defined for the present Rankine-type vortex in § 2.3.

The wave energy propagates along rays defined by the ray equations

$$\frac{\mathrm{d}\boldsymbol{x}}{\mathrm{d}t} = \boldsymbol{U} + \boldsymbol{v}_g, \tag{2.13}$$

where $\boldsymbol{v}_g$ is the intrinsic group velocity of the wave, of which the components are given by the formula

$$v_{gx} = \frac{N^2 - \omega_o^2}{\omega_o k^2} k_x, \quad v_{gy} = \frac{N^2 - \omega_o^2}{\omega_o k^2} k_y, \quad v_{gz} = -\frac{\omega_0^2 - f^2}{\omega_0 k^2} k_z, \tag{2.14}$$

where k is the norm of the wave vector $\boldsymbol{k}$. Using the Doppler relationship, the refraction equations become in Newtonian notation

$$\frac{\mathrm{d}k_i}{\mathrm{d}t} = -\frac{N}{\omega_o} \left(\frac{\omega_o^2 - f^2}{N^2 - f^2} \right) \frac{\partial N}{\partial x_i} - \sum_{j=1}^{3} k_j \frac{\partial U_j}{\partial x_i}, \tag{2.15}$$

representing the evolution of the wavenumber components along a ray.

Equation (2.13) shows that, according to WKB theory, the wave energy is advected by the local fluid velocity $\boldsymbol{U}$, and that the Doppler effect (1.1) is interpreted in (2.15) as a distortion of the wavenumber vector by the variations in buoyancy frequency and by the local background shear. Integration of the set of ordinary differential equations (2.13) and (2.15) from an initial state, defined by a position vector $\boldsymbol{r}_o$ and

incident wave characteristics $\boldsymbol{k}_o$, gives the ray along which the wave energy propagates as well as the evolution of the wave characteristics along this ray.

Another equation is required to predict the evolution of the wave amplitude along the ray. This amplitude is proportional to A in equations (2.12). Bretherton (1966) showed that the higher-order equations that drive the amplitude evolution in the WKB approximation, could be simplified to:

$$\nabla \cdot \left[(\boldsymbol{v}_g + \boldsymbol{U}) \frac{E}{\omega_o} \right] = 0, \tag{2.16}$$

describing the energy evolution. The local density of energy, E, is defined as $E = 1/2(\tilde{u}^2 + \tilde{v}^2 + \tilde{w}^2 + \tilde{b}^2/N^2)$ where $\tilde{u}$, $\tilde{v}$, $\tilde{w}$ and $\tilde{b}$ are the velocity and buoyancy parts of the wave field, and is linked to the amplification factor A by the relation

$$E = \left(A\omega_0 \frac{k_h}{k_z} k \right)^2.$$

For a tube of rays, equation (2.16) represents the flux conservation of the wave action, E/ω_o, along the tube. When the tube-section area decreases, flux conservation leads to an increase of the wave-action. Therefore, the wave-action increases (decreases) when rays converge (diverge).

Generally, in studies on parallel shear flows based on the conservation of the wave number component parallel to the background flow, the intrinsic frequency ω_o depends only on the spatial position; critical layers are well defined and are exactly the same for all rays forming an initially parallel tube. When a wave approaches a critical layer, the cross-sectional area of the ray tube goes to zero and the conservation of wave-action flux, described by equation (2.16), leads to an infinite amplification of the energy E. This explanation does, however, not hold for flows with curvature since each ray approaches its own critical layer leading to a finite amplification of energy.

2.3. *Ray propagation into a vortex velocity field*

We consider an isolated Rankine vortex characterized by a core of constant cyclonic vorticity of radius R, embedded in a ring of constant anticyclonic vorticity such that the total circulation vanishes at radius L. In the vertical direction, we suppose a Gaussian distribution of vertical vorticity with a vertical length scale H. We consider stable vortices with $L/R = 2$ (see Flierl 1988). The fluid is linearly stratified, has a buoyancy frequency, N_o, and a rotation frequency, Ω, implying a Coriolis parameter $f = 2\Omega$. The strength of the vortex is determined by its maximum velocity U_{max}, so that the azimuthal velocity field U reads

$$U(r, z) = U_{max} \exp(-(z/H)^2) \begin{cases} \dfrac{r}{R} & \text{if } 0 < r < R, \\ \dfrac{1}{1 - (R/L)^2} \left(\dfrac{R}{r} - \left(\dfrac{R}{L} \right)^2 \dfrac{r}{R} \right) & \text{if } R < r < L. \end{cases} \tag{2.17}$$

The density field for this vortex can be deduced from the thermal-wind relation obtained from (2.4)–(2.5),

$$\frac{g}{\rho_o} \frac{\partial \rho_v}{\partial r} = -\left(f + \frac{2U}{r} \right) \frac{\partial U}{\partial z}. \tag{2.18}$$

The WKB theory applies well to the outer region which is in geostrophic balance, but is a crude approximation in the core region of the vortex which is in cyclostrophic

balance, i.e. where the second term on the right-hand side of (2.18) is large compared to the first. As stated before, the forbidden region for rays covers the core region of the vortex and rays almost never penetrate the vortex centre. Only rays that propagate close to the vortex axis do not feel the relatively weak velocity there and traverse vortex structure with almost no modification. Therefore, we do not consider these rays and neglect the cyclostrophic term that is important in the vortex core in (2.18). Then the density field ρ_v reads

$$\rho(r,z) = \int_r^L \frac{\partial U}{\partial z}\left(\frac{f\rho_o}{g}\right) \mathrm{d}r'. \tag{2.19}$$

The discrepancies with the exact density field prescribed by (2.18) are important only near the vortex centre.

With equations (2.17) and (2.19) an analytical expression for the buoyancy frequency field inside the vortex can be derived, which after scaling with background buoyancy frequency N_o, becomes

$$N^{*2} = \frac{N^2(r,z)}{N_o^2} = 1 + \frac{fU_{max}R}{H^2N_o^2}(1-2(z/H)^2)\exp\left(-\left(z/H\right)^2\right) \times \begin{cases} -\left(\dfrac{r}{R}\right)^2 + \dfrac{2\ln(L/R)}{1-(R/L)^2} & \text{if } 0 < r < R, \\ \dfrac{2\ln(L/r) - 1 + (r/L)^2}{1-(R/L)^2} & \text{if } R < r < L. \end{cases} \tag{2.20}$$

The velocity field of the vortex is completely described by (2.17) and (2.20). After transformation into a cylindrical reference frame (see Appendix) and substitution into the set of ray and refraction equations (2.13) and (2.15), the propagation of inertia–gravity waves can be described in cylindrical coordinates. Scaling all lengths with the vortex core radius R and time with N_o, we obtain a non-dimensional set of equations:

$$\frac{\mathrm{d}r}{\mathrm{d}t} = \frac{N^{*2}-\omega_o^2}{\omega_o k^2}k_r, \tag{2.21}$$

$$\frac{\mathrm{d}\theta}{\mathrm{d}t} = \frac{1}{r}\left(\frac{N^{*2}-\omega_o^2}{\omega_o k^2}k_\theta + FrU^*\right), \tag{2.22}$$

$$\frac{\mathrm{d}z}{\mathrm{d}t} = -\frac{\omega_o^2-(f/N_o)^2}{\omega_o k^2}k_z, \tag{2.23}$$

$$\frac{\mathrm{d}k_r}{\mathrm{d}t} = -Fr\frac{f}{N_o}\left(\frac{R}{H}\right)^2\frac{\omega_o^2-(f/N_o)^2}{\omega_o(N^{*2}-\omega_o^2)}\left(N^*\frac{\partial N^*}{\partial r}\right) - Frk_\theta\left(\frac{\partial U^*}{\partial r} - \frac{U^*}{r}\right) + \frac{k_\theta}{r}\frac{N^{*2}-\omega_o^2}{\omega_o k^2}k_\theta, \tag{2.24}$$

$$\frac{\mathrm{d}k_\theta}{\mathrm{d}t} = -\frac{k_\theta}{r}\frac{N^{*2}-\omega_o^2}{\omega_o k^2}k_r, \tag{2.25}$$

$$\frac{\mathrm{d}k_z}{\mathrm{d}t} = -Fr\frac{f}{N_o}\left(\frac{R}{H}\right)^4\frac{\omega_o^2-(f/N_o)^2}{\omega_o\left(N^{*2}-\omega_o^2\right)}\left(N^*\frac{\partial N^*}{\partial z}\right) - Fr\left(\frac{R}{H}\right)^2 k_\theta\left(\frac{\partial U^*}{\partial z}\right). \tag{2.26}$$

Field	$f(r)$ for $r<1$	$f(r)$ for $1<r<L/R$	$g(z)$
U^*	r	$\frac{1}{1-(R/L)^2}\left(\frac{1}{r}-\left(\frac{R}{L}\right)^2 r\right)$	$\exp(-(R/H)^2 z^2)$
$\frac{\partial U^*}{\partial r}-\frac{U^*}{r}$	0	$-\frac{1}{1-(R/L)^2}\left(\frac{2}{r}\right)$	$\exp(-(R/H)^2 z^2)$
$\frac{\partial U^*}{\partial z}$	r	$\frac{1}{1-(R/L)^2}\left(\frac{1}{r}-\left(\frac{R}{L}\right)^2 r\right)$	$-2z\exp(-(R/H)^2 z^2)$
$N^*\frac{\partial N^*}{\partial r}$	$-r$	$\frac{1}{1-(R/L)^2}\left(-\frac{1}{r}+\left(\frac{R}{L}\right)^2 r\right)$	$\left(1-2\left(\frac{R}{H}\right)^2 z\right)\exp(-(R/H)^2 z^2)$
$N^*\frac{\partial N^*}{\partial z}$	$-r^2+\frac{2\ln(L/R)}{1-(R/L)^2}$	$\frac{1}{1-(R/L)^2}\left(2\ln\left(\frac{L}{R}\right)-2\ln(r)-1+\left(\frac{R}{L}\right)^2 r^2\right)$	$-z\left(3-2\left(\frac{R}{H}\right)^2 z^2\right)\times\exp(-(R/H)^2 z^2)$

TABLE 1. Non-dimensional analytical expressions for the different components of the cyclonic vortex field. The functions $f(r)$ and $g(z)$ correspond, respectively, to the radial and vertical parts of the field.

The variable Fr is the Froude number defined as above, $Fr = U_{max}/N_o R$, whereas N^* and U^* are the non-dimensionalized buoyancy frequency and velocity, respectively. Both, N^* and U^* are written as functions of $f(r)g(z)$ of which the analytical expressions for a cyclonic vortex with $U_{max}>0$ are given in table 1. The intrinsic frequency in the non-dimensional dispersion relation

$$\omega_o^2 = \frac{N^{*2}\left(k_r^2+k_\theta^2\right)+(f/N_o)^2 k_z^2}{k^2}, \tag{2.27}$$

is a function of the components of the wave vector and the buoyancy frequency field, while the non-dimensional form of the Doppler shifting relationship now reads

$$\omega_{abs} = \omega_o + Frk_\theta r\left(\frac{U}{r}\right), \tag{2.28}$$

where for convenience the asterisks are dropped.

Equation (2.25) implies the conservation of $k_\theta r$ along a ray (see Appendix) so that, with (2.28), ω_o depends only on the spatial position (r, z). The shear-driven terms in equations (2.24) and (2.26) are derivatives of the component U/r, i.e. $\partial(U/r)/\partial r = 1/r(\partial U/\partial r - U/r)$. This component has the same meaning as the velocity field U for a parallel shear flow in Cartesian coordinates. However, the rays of an incident planar wave in a cylindrical frame of reference have different values of $k_\theta r$, implying a different behaviour.

To consider the last term on the right-hand side in (2.24) in more detail, we derive the evolution equation for the horizontal component of the wave vector, $k_h = \sqrt{k_r^2+k_\theta^2}$,

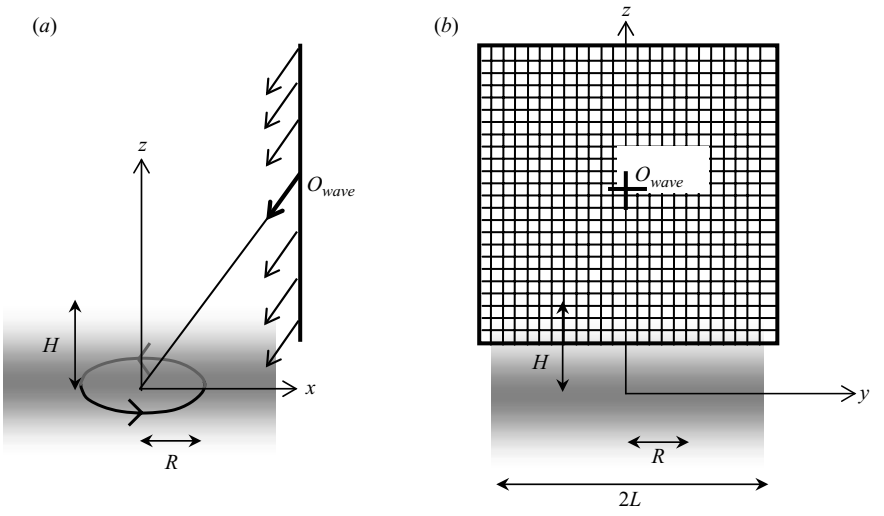

FIGURE 1. Sketch of the initial position of the incident parallel rays used for the WKB simulations with respect to the vortex of which the vorticity amplitude is represented by grey intensity. (*a*) The side view showing the position and relative size of the vortex and (*b*) the backward view of the grid of size relative to the vortex. In the text the dimensions are scaled with R. The central ray in the grid, located in O_{wave}, propagates towards the centre of the vortex. In (*b*), the vortex is in the background.

from (2.24) and (2.25),

$$\frac{\mathrm{d}k_h^2}{\mathrm{d}t} = -Fr\frac{f}{N_o}\left(\frac{R}{H}\right)^2 \frac{k_r}{2}\frac{\omega_o^2-(f/N_o)^2}{\omega_o\left(N^2-\omega_o^2\right)}\left(N\frac{\partial N}{\partial r}\right) - Fr\frac{k_\theta k_r}{2}\left(\frac{\partial U}{\partial r}-\frac{U}{r}\right). \qquad (2.29)$$

We recognize in (2.29) the linear propagation of internal waves in a fluid at rest (i.e. $Fr=0$) for which k_h remains constant. As a consequence, in a cylindrical coordinate system where rk_θ is conserved, k_r must evolve to maintain k_h constant. In the core region of the vortex ($r<1$), described by (2.17), $U/r-\partial U/\partial r=0$, so that the evolution of k_h is only driven by the radial gradient of N.

To solve (2.21)–(2.26), we prescribe the incident planar wave as a superposition of initially parallel rays with identical frequencies, ω_{abs}, and wavenumber, k. The dispersion relationship determines the different components of the wave vector. Only rays which interact with the vortex velocity field are considered, so that the numerical resolution can be carried out for a regular grid of rays of finite dimension. The position of the grid of incident rays relative to the vortex flow is shown in figure 1, where the centre of the grid, noted O_{wave}, corresponds to the ray aiming at the centre of the vortex. The horizontal and vertical steps were chosen such that the 10 000 incident rays are equally spaced on the grid. For each ray, the WKB equations (2.21)–(2.26) are solved, using a fourth-order Runge–Kutta algorithm applied to the five-component vector (r, θ, z, k_r, k_z) with rk_θ being conserved. The intrinsic frequency, ω_o, is deduced from the dispersion relationship (2.27), and the Doppler-shifting relationship (2.28) is used to double-check the accuracy of the numerical scheme. In the WKB theory, the two relationship are fulfilled, and the numerical solution must be accurate enough to respect this constraint.

In order to detect the trapping of incident rays, the numerical integration should be continued for a sufficiently long period of time. For a simulation with rays of

absolute frequency ω_{abs} and wavenumber k, we define the reference time, t_{ref}, as the time it takes for the wave to propagate a horizontal distance equal to the vortex radial extent, $2L/R$, in the absence of a vortex. Simulations that lasted around $8t_{ref}$ were long enough to distinguish rays trapped in the vortex velocity field from escaping rays, and therefore this time limit is the one used in numerical simulations presented below.

3. Numerical results for the inviscid propagation

In order to investigate the wave propagation, we have divided the vortex region into three regions, with $0 < r < 1$ representing the core with positive vorticity, $1 < r < 2$ representing the ring with negative vorticity, and $r > 2$ the exterior at rest. The waves are emitted from the grid points in figure 1(*b*). The frequency of a wave and implicitly its direction may change owing to the presence of the shear flow by the Doppler effect as can be inferred from relation (2.28). This Doppler shift is the major physical effect at work. The strength of the Doppler shift in (2.28) is measured by kFr, since $r(U/r)$ is around unity and k_θ is proportional to the non-dimensional wavenumber k. The length scale is prescribed by the vortex radius R, whereas the wavelength λ can take any value, so that the non-dimensional wavenumber $k = 2\pi R/\lambda$ belongs to $[-\infty, +\infty]$.

We distinguish waves propagating in the direction parallel to the azimuthal velocity field of the vortex (i.e. $k_\theta > 0$, or 'with the flow') and waves propagating in the opposite direction to this velocity field (i.e. $k_\theta < 0$, or 'against the flow'). Rays propagating against the flow (with the flow) experience an increase (decrease) in intrinsic frequency. The intrinsic frequency range is delimited by the layers where ω_o reaches values equal to f/N_o or 1. The expression for these layers can be deduced from the Doppler shift and the conservation of rk_θ and are given by $r_o k_{\theta o}(U(r,z)/r) = 1$ and $r_o k_{\theta o}(U(r,z)/r) = f/N_o$, where r_o and $k_{\theta o}$ are the initial values of r and k_θ for the ray.

3.1. *Behaviour of rays and definition for the trapping of rays*

When $kFr \ll 1$, only the intrinsic frequency ω_o, and implicitly the orientation of the rays are weakly modified. Increasing kFr to $O(1)$ shows that some rays reflect and strongly interact with the vortex. For still higher values of kFr, some rays remain inside the vortex even for large times and exhibit a strong decrease in wavelength, associated with the trapping along a critical layer. Since the vortex is confined in space, these interacting rays escape eventually, in contrast to rays interacting with infinite jets (see Olbers 1980). Therefore, we define the decrease in wavelength up to one-tenth of the initial value as a criterion for trapping. This decrease in wavelength is proportional to a decrease of the intrinsic group velocity implying partial trapping of wave energy inside the vortex. The threshold value for the decrease in wavelength is deduced from the evolution of the wavenumber spectra with time, and will be justified at the end of this section.

Figure 2 shows the distribution of trapped rays plotted in the incident grid defined in figure 1(*b*). Rays propagating against the flow, $k_\theta < 0$, are marked by grey circles in figure 2. The rays denoted *a*–*g* differ from each other in initial height, whereas a typical ray propagating along the flow, $k_\theta > 0$, is denoted *h*. Figure 3 shows a three-dimensional view of the ray *d*, and illustrates how it wraps around the vortex structure while being trapped. Note that wave breaking or viscous effects may prevent this ray from eventually escaping the vortex shear flow. In figure 4, these rays are

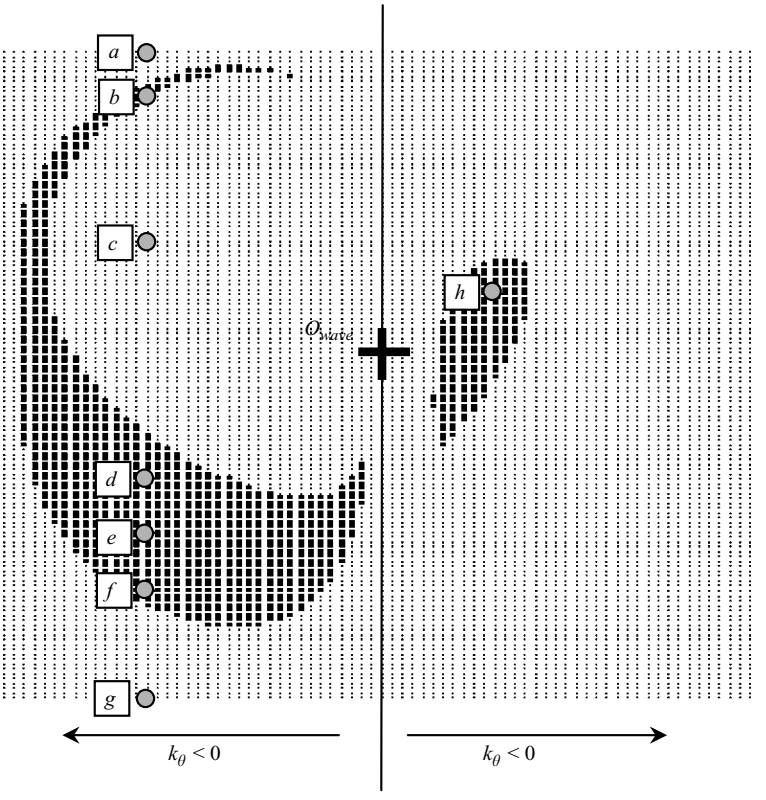

FIGURE 2. Distribution of rays in the grid in figure 1(*b*) that will be trapped in the vortex: thick dots mark trapped rays. Grey circles labelled (*a–h*) indicate the locations of rays that are plotted in figure 4 and are discussed in the text. For this simulation, the parameters are: $H/R = 1.0$, $L/R = 2.0$, $f/N_o = 0.1$, $Fr = 0.1$, $k = 31.0$ and $\omega_{abs} = 0.85$. The numbers of nodes on the regular grid are 74 and 134 in the horizontal and vertical directions, respectively, corresponding to about 10 000 incident parallel rays.

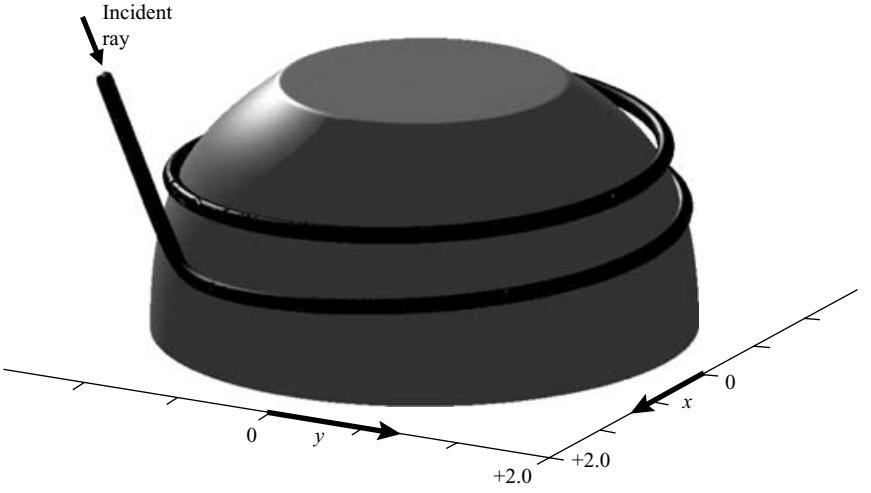

FIGURE 3. Three-dimensional view of the ray labelled d in figure 2. The grey volume is the upper half of the forbidden region for this ray (see text).

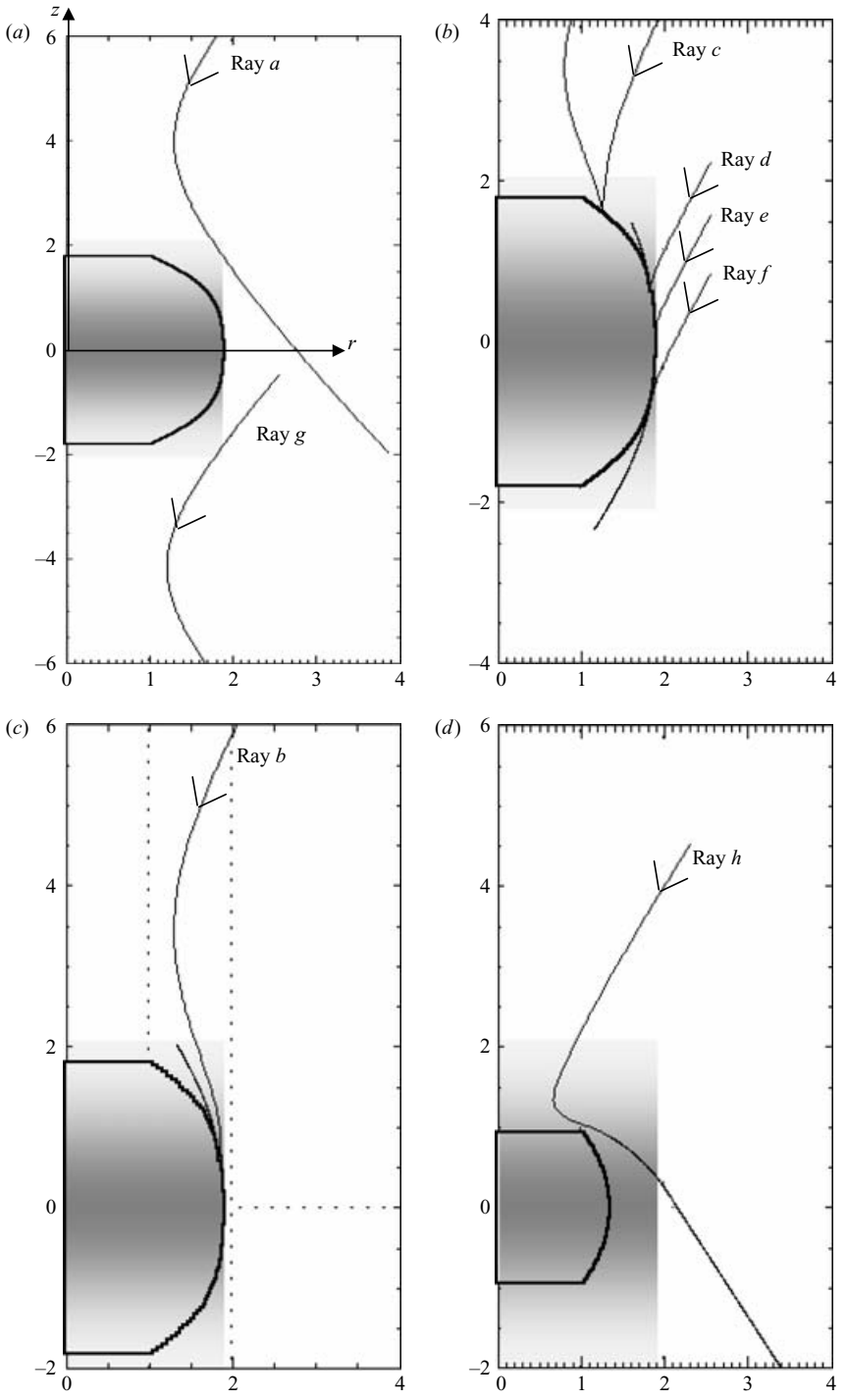

FIGURE 4. Typical behaviour of the rays labelled in figure 2, here plotted in the (r, z)-plane. The vortex is represented in grey-colour, with the gradient representing the gradient in horizontal velocity with $z \in [-H/R, H/R]$. Forbidden regions where ω_o is outside the range $[f/N_o, 1]$ (see text) are delimited by bold lines. Rays a–h have been grouped in different figures, depending on their behaviour (see text). The parameters of the simulation are the same as in figure 2.

plotted in the (r, z)-plane; the gradient in the amplitude of the vortex velocity field is displayed by the gradient in grey colour. For each ray, the boundary of the forbidden region mentioned above is indicated by a solid line. This boundary is exactly the same for rays *a*–*g* since they have the same value of rk_θ.

For $k_\theta < 0$, rays propagating in the far field, illustrated by *a* and *g* in figure 4(*a*) experience a weak shift in intrinsic frequency ω_o, which remains close to ω_{abs}. Conservation of rk_θ and very weak change of k_h lead to a constant increase of the radial component k_r, from negative values towards positive values, explaining the presence of turning points in figure 4(*a*). At these points, $k_r = 0$ and r is equal to the minimal distance of the ray to the centre of the cylindrical coordinate system. In top and side views, these rays would appear as very weakly curved lines, the wave energy being slightly advected during propagation through the vortex region $r < L/R$.

The rays *c*, *d*, *e* and *f* illustrated in figure 4(*b*) propagate against the flow and penetrate into the vortex. We consider each case separately. Ray *c*, after reflecting on the layer $\omega_o = N$, penetrates inside the core region ($r < 1$). The radial wavenumber stretching, proportional to $U/r - \partial U/\partial r$, is equal to zero by the choice of our velocity field, so that this ray behaves as in a parallel flow with vertical shear and eventually escapes. Rays *d*, *e* and *f* propagate relatively slowly, and are trapped in the zone where $\omega_o = N$, close to the vertical, where the radial shear is intense. They propagate very slowly in comparison with rays *a* and *g*, while their wavelength becomes smaller than one-tenth of the initial value. Ray *f* misses the reflection layer and crosses the mid-plane ($z = 0$), but propagates in the outer region with an orientation leading to a fast increase of the radial and vertical wavenumber components. Ray *b* in figure 4(*c*) first turns back towards to the layer $\omega_o = N$, where it subsequently reflects and becomes trapped, similar to ray *d*. Only a small section of the incident wave field in figure 2 shows this complicated behaviour.

Rays propagating with the flow ($k_\theta > 0$) and having a turning point located in the outer region experience only a modest change in wavelength and escape from the vortex. Only rays with low absolute values of k_θ, such as ray *h* in figure 4(*d*), which would propagate without interaction near the vortex centre, are able to penetrate inside the core region $r < 1$. There, the gradient in U/r is only vertical so that the ray propagation is very similar to that in a purely vertical shear flow: rays are gradually trapped along the horizontal critical layer defined by $\omega_o = f/N_o$. Rays such as *h* in figure 4(*d*) penetrate inside the vortex core region, experience a relatively effective decrease in wavelength compared to waves that only cross the outer region (see figure 2).

Figure 5(*a*) shows the spatial distribution of all rays near the vortex for $kFr = 3.1$, at time $t = 8t_{ref}$. The rays plotted in the left-hand part of figure 5(*a*) slowed down during the interaction, and were eventually trapped. Rays in the outer region ($1 < r < L/R$) that propagate against the flow ($k_\theta < 0$), are located in a region with strong radial and vertical shear, so that their wavelength will keep on decreasing. Rays in the core region, $r < 1$, also propagate against the flow, but escape the intense radial shear region at $r = 1$, without a further decrease in wavelength. The lower-right part of figure 5(*a*) shows rays which propagate with the flow ($k_\theta > 0$), corresponding to rays such as *h* in figure 4(*d*). The corresponding zoom out in figure 5(*b*) shows that most rays propagate to the lower-left part of the figure. The rays in the upper-right part of the figure correspond to rays of type *c* in figure 4(*b*), and propagate upward. They reflect on the layer $\omega_o = N$ before escaping the vortex velocity field. The bold vertical segment in figure 4 indicates where the rays would be located in the absence of the vortex. Figure 6 represents a three-dimensional view of the final positions of

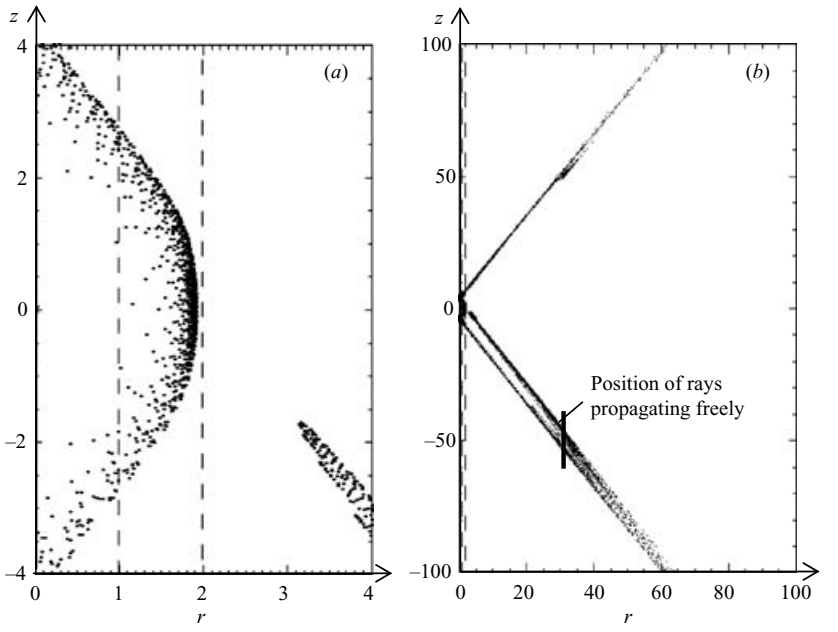

FIGURE 5. (*a*) Ray positions in the (r, z)-plane for the simulation in figure 2 at $t = 8t_{ref}$, and (*b*) a zoom out of the same plot. In (*a*), the dashed lines indicate the limits between the core, $r = 1$, and the outer boundary of the vortex, $r = L/R = 2$. In (*b*), the bold vertical segment indicates the position in the absence of a vortex.

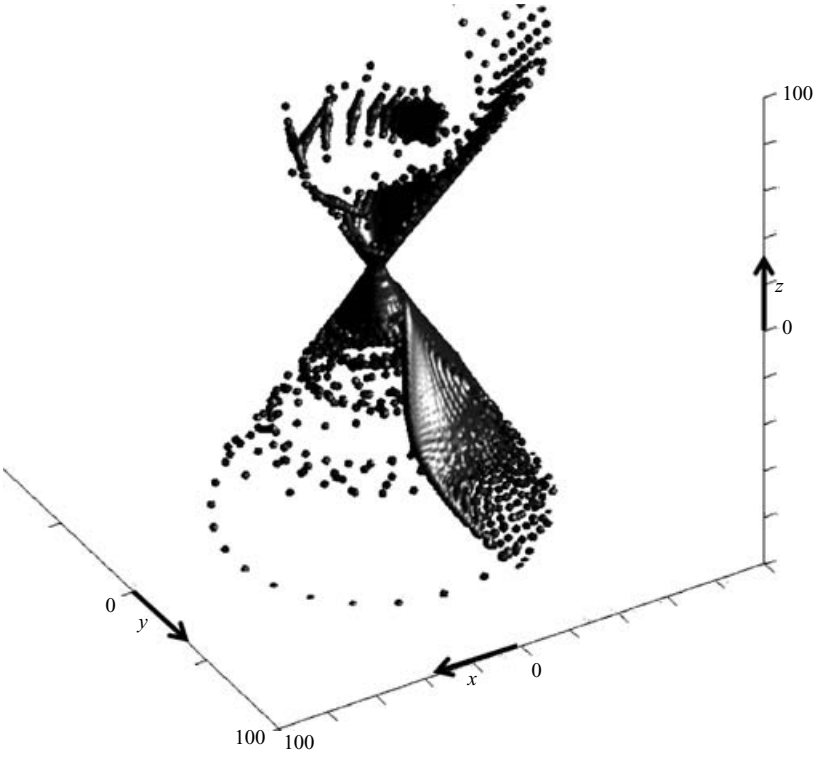

FIGURE 6. Three-dimensional view of the final position of rays, at $t = 8t_{ref}$, for the simulation of figure 2.

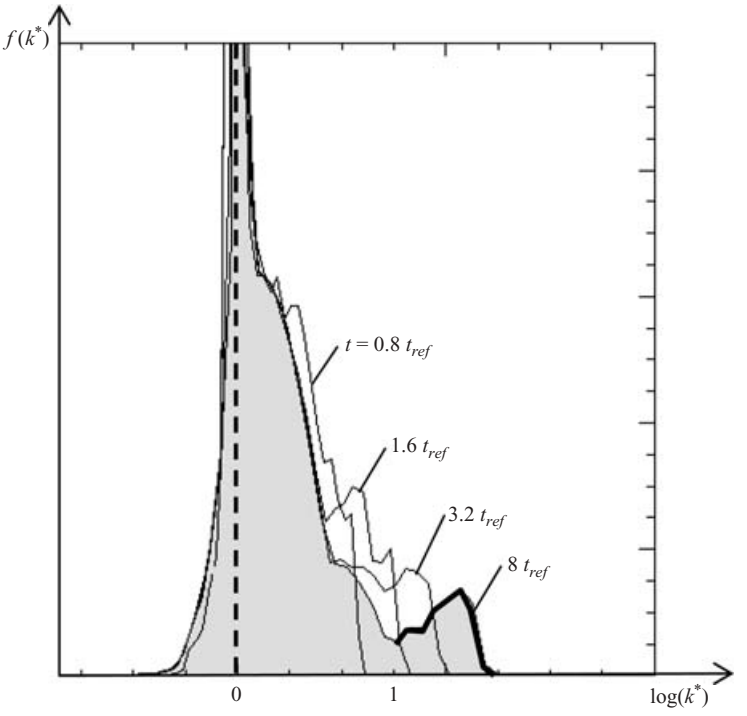

FIGURE 7. Evolution with time of the wavenumber distribution for rays in the simulation of figure 2. k^* is the ratio between the wavelength at time t and its initial value. The bold vertical line indicates the distribution of the wavenumbers at the beginning of the simulation. Time $t = 8t_{ref}$ is the distribution at the end of the simulation. The bold line on the right-hand side indicates the location of rays of which the final wavelength is smaller than one-tenth of the initial value, represented by bold dots in figure 2.

the rays, and shows that even rays that are not trapped, are strongly deflected by the interaction. We can infer from the dispersion relationship, that the energy of escaping waves still propagates along a cone-shaped surface (the axisymmetric equivalent of the St Andrew's cross of gravity waves in a fluid at rest, see Turner 1973), but the initially planar wave structure is entirely deformed.

The temporal evolution in the wavenumber distribution of the interacting rays is shown in figure 7. The asymmetric distribution around the initial value ($\log(k^*) = 0$) represents the waves that are affected by the shear and escape (see curve $t_c = 1.6t_{ref}$ in figure 7). Some rays exhibit a decrease of their wavenumber ($\log(k^*) < 0$ in the figure) since for fixed values of k_θ and ω_{abs}, the dispersion relation gives different pairs of (k_r, k_z), of which some have a final wavenumber lower than that of the incident ray. These rays have a higher group velocity and appear in the lower-right part of figure 5(b). The trapped rays correspond to the wavenumbers which increase linearly with time and eventually form a 'packet' of wavenumbers visible on the right part of figure 7 for $t = 8\ t_{ref}$, illustrated by a bold line. The separation of this packet from the wavenumbers of the escaping rays occurs around $\log(k^*) = 1$. This corresponds to the decrease in wavelength to one-tenth of the initial value that we used to define trapping.

3.2. *Influence of vortex shape on wave propagation*

In order to investigate the effect of the vortex characteristics on the trapping, the vortex aspect-ratio H/L was varied for different values of N/f and Fr. Simulations

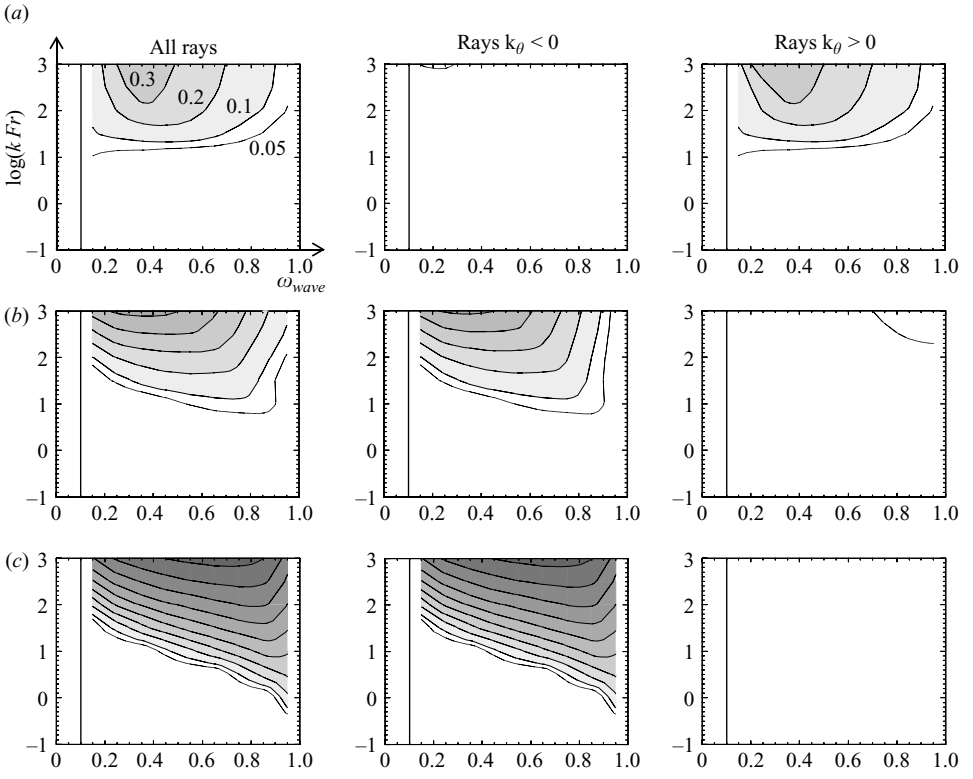

FIGURE 8. Contours of the trapping section, σ, for vortices with different aspect ratios H/R: (*a*) $H/R = 0.1$, (*b*) $H/R = 1.0$, (*c*) $H/R = 5.0$ and constant parameters $f/N_o = 0.1$, $L/R = 2.0$, $Fr = 0.1$. Figures on the left-hand side are calculated by taking account of all rays. Figures in the middle and on the right-hand side show contributions from rays propagating against the flow, or along it, respectively. Thick lines are contours of $\sigma = 0.05$, 0.1, then with intervals of 0.1.

were carried out for values of k between 0.1 to 1000.0 and ω_{abs} in the range $[f/N_o, 1]$. To estimate the impact of the vortex shape on the trapping, we define σ_{vortex} as the area of the vortex seen by incident rays of frequency ω_{abs}. For the vortex defined by (2.7) with aspect ratio H/R, we take H as a typical vertical extent of the vortex. The vortex area, σ_{vortex}, made non-dimensional by R is given by the radius L/R, the area of the grid of rays, a rectangle of $2H/R$ by $2L/R$, and the direction of the waves between the limits $\omega_{abs} = 1$ and $\omega_{abs} = f/N_o$, respectively, and reads

$$\sigma_{vortex}\left(\omega_{abs}, \frac{H}{R}, \frac{L}{R}\right) = \frac{L}{R}\left(4.0\frac{H}{R}\sqrt{\frac{1-\omega_{abs}^2}{1-(f/N_o)^2}} + \pi\frac{L}{R}\sqrt{\frac{\omega_{abs}^2-(f/N_o)^2}{N^2-(f/N_o)^2}}\right).$$

We define σ as the area of trapped rays divided by the vortex area σ_{vortex}. In figure 8, contours of the trapping area σ, have been plotted as a function of kFr and ω_{abs} for vortices with different aspect ratios, while other non-dimensional parameters are kept fixed. The different scenarios found for $k_\theta < 0$ and $k_\theta > 0$ and the vortex shape are discussed below.

For flat vortices, rays propagating with the flow (ray h in figure 4*d*) are trapped by the strong vertical shear $\partial(U/r)/\partial z$ (see figure 8*a*, $H/R = 0.1$), while rays propagating against the flow escape (rays $c - f$ in figure 4*b*). Only for short waves does the

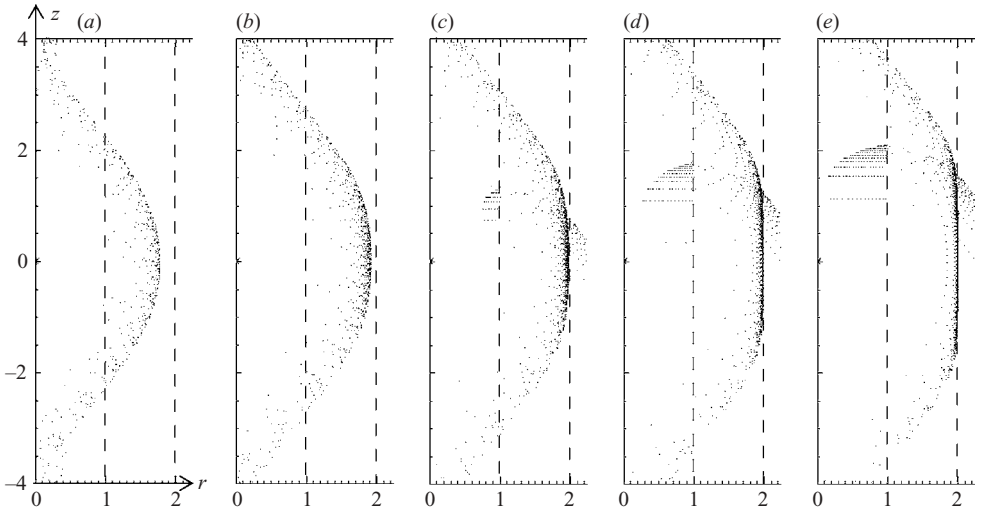

FIGURE 9. Trapped rays, plotted in the meridional (r, z)-plane for increasing value of k: (*a*) $k = 10.0$, (*b*) $k = 31.0$, (*c*) $k = 100.0$, (*d*) $k = 310.0$, (*e*) $k = 1000.0$. Other parameters are kept fixed and are equal to: $L/R = 2.0$, $H/R = 1.0$, $f/N_o = 0.1$, $\omega_{abs} = 0.85$ and $Fr = 0.1$.

curvature of the flow becomes negligible, and some rays propagating against the flow are eventually trapped when approaching the frequency $\omega_{abs} \approx 0.2$, as in a geostrophic jet (see Olbers 1980). These rays are trapped near the edge of the vortex, $(z, r) = (0, L)$, where the horizontal shear is dominant and the critical-layer condition, $\omega_o = N$, is met.

For tall vortices, $H/R = 5.0$, waves propagating with the flow reflect and escape, while waves propagating against the flow are trapped along almost vertical critical layers that are, as above, located near the reflection layer $\omega_o = N$ (see figure 8*c*). In contrast to flat vortices, even short waves (high kFr) propagating along the flow escape after reflection in the region $1 < r < 2$. Only smaller values of $H/R = 1.0$, allow some rays that propagate along the flow to penetrate inside the core region, where they can exhibit stretching in wavenumber (see figure 8*b*).

For decreasing wavelengths (increasing kFr) and rays propagating against the flow, the trapping region gradually becomes closer to the outer part of the vortex and increases in density, i.e. the final distance between two neighbour trapped rays decreases (see figure 9). Conservation of the wave-action flux expressed by (2.16), will then lead to an energy amplification which grows with kFr. In real flows, this energy amplification is balanced by diffusive damping or nonlinearities. In an attempt to compare quantitatively the opposing effects of trapping and viscous damping, we consider the energy evolution for a single ray trapped in the outer part of the vortex, adopting a simpler flow model.

4. Combined effects of curvature and viscosity for trapped rays

The rays that penetrate into the vortex and are subsequently trapped, like ray *d* in figure 4(*b*), typically feel a baroclinic horizontal and vertical shear given by, respectively, $U_L = U_{max}/(L - R)$ and $U_H = U_{max}/H$. The effect of the velocity field on the rays is then locally the same as the effect of a constant shear, and leads to a linear decrease of the wavelength with time. As the wavelength decreases, the viscous damping rate increases accordingly and eventually overcomes the energy amplification.

In order to investigate the effects of both curvature and viscosity on the energy amplification of a ray trapped in the vortex, we will consider a simplified azimuthal velocity field instead of (2.7), with the same shear intensity, but parallel iso-velocity surfaces. This allows for an easier comparison with the results obtained by Olbers (1980) for a geostrophic jet. This simplified velocity field reads

$$U(r,z) = U_{max} \begin{cases} -\dfrac{1}{L-R}(r-L) - \dfrac{1}{H}z & \text{for } \dfrac{1}{L-R}(L-r) + \dfrac{1}{H}z < 0, \\ 0 & \text{for } \dfrac{1}{L-R}(L-r) + \dfrac{1}{H}z > 0, \end{cases} \tag{4.1}$$

where U_{max}, R, L and H are the parameters for the vortex velocity field. In this flow, the isopycnals are inclined owing to the vertical shear, but the derivatives of N are equal to zero. This approach is justified since the buoyancy term in (2.21)–(2.26) is negligible in comparison with the effect of the shear for a ray with large kFr that is trapped in the periphery of the vortex.

Note that equations (4.1) represent a simplified approximation of the shear flow of the vortex periphery (2.17) and that the divergence for $r \to 0$ or $(r,z) \to \infty$ is not concerned. Rays remain close to their point of penetration in the (r,z) plane, i.e. in the vortex periphery.

To study the energy amplification during the trapping, the WKB equations in the cylindrical reference frame (2.21)–(2.26) are solved for a set of initially parallel rays distributed along a tube. The cross-section of this tube represents the wave action flux, which is proportional to the energy. Under the inviscid assumption represented by (2.16), the wave action is conserved and the tube has a constant cross-sectional area.

To calculate the energy evolution along the ray, and taking account of viscosity, we use a modified version of the wave-action equation (2.16), given by (see Booker & Bretherton 1967)

$$\nabla \cdot \left[\left(\boldsymbol{v}_g + \boldsymbol{U} \right) \frac{E}{\omega_o} \right] = -\nu k^2 \frac{E}{\omega_o}, \tag{4.2}$$

where ν is the viscosity of the fluid and k is the norm of the wavenumber. In contrast to the inviscid case, the wave action which is proportional to the cross-section of the ray tube, decreases along the ray. The dissipation rate along a ray (right-hand side of (4.2)) is evaluated numerically from the volumes of the successive portions of the tube.

Figure 10 displays meridional and top views of a ray propagating against a baroclinic flow with an initial incident angle $\alpha = 3\pi/4$ with the azimuthal velocity. The baroclinic shear is given by $U_L/U_H = H/(L-R) = 4$ and $f/N_o = 0.1$. As for ray d in figure 4(b), the ray first reflects on a reflection layer where $\omega_o = N$ (at $z = -0.35$) and is then trapped along a critical layer, similarly to the ray trapping in a baroclinic geostrophic jet studied by Olbers (1980). Olbers (1980) showed that the rays in this jet propagate in a wave guide of which the thickness, δ, is deduced from the Doppler shifting relationship and reads $\delta = (N_o - f)/k_\theta \sqrt{U_L^2 + U_H^2}$. When divided by L, its non-dimensional form is:

$$\frac{\delta}{L} = \frac{(1 - f/N_o)}{\sqrt{(R/(L-R))^2 + (R/H)^2}(k_\theta/k)} \left(\frac{1}{kFr} \right), \tag{4.3}$$

where k_θ/k depends only on ω_{abs} and α. This expression shows how an increase of kFr for a fixed configuration (L/R, w_{abs} and α maintained constant) corresponds to a decrease in wave-guide thickness relative to the horizontal extent of the vortex. The jet studied by Olbers (1980) is recovered in the limit $\delta/L = 0$, or equally $kFr = \infty$.

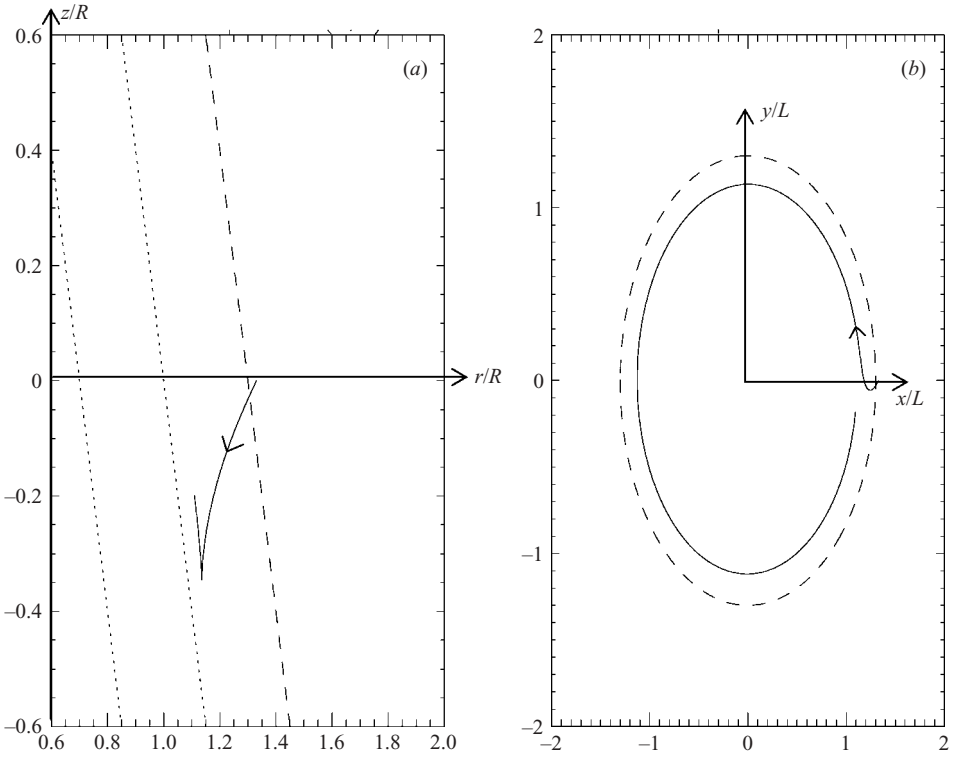

FIGURE 10. (*a*) Ray propagating in front of a weakly baroclinic constant shear flow ($U_L/U_H = 4$) in the (r, z)-plane and (*b*) top view. ——, ray; – – –, limit of the non-zero velocity field; · · ·, iso-velocity surfaces. Lengths are scaled with R and $L/R = 1.3$.

In figure 11(*a*), the inviscid evolution of the energy from the beginning of the interaction is plotted for different values of δ/L and for the Cartesian limit $\delta/L = 0$. The sharp peak observed in the curves δ/L corresponds to the reflection of waves on the layer $\omega_o = N$, where the WKB approximation predicts an infinite amplification of energy.

In the limit $\delta/L \to 0$, all the rays of the tube are trapped at the same critical level, and the area of the tube cross-section tends to zero as time tends to infinity, leading to an unlimited growth of the wave energy. For a finite value of the curvature δ/L, each ray converges to its own critical level, and the cross-section of an initially circular tube of rays takes an elliptical shape. In figure 11(*a*), the energy evolution is plotted against time for different values of δ/L. The curves with $\delta/L > 0$ tend to a finite value of the energy with $\delta/L > 0$. Accordingly, figure 12 displays the final elliptical shape of the cross-sections of the ray-tube for different values of δ/L; the cross-section tends to zero for $\delta/L \to 0$. Waves are trapped in the mean flow and the wavelength decreases with time in parallel shear flow, but the energy reaches a finite value. This narrowing of the section area of the tube of rays with the parameter δ/L corresponds to the narrowing of the trapping region with increasing kFr observed in WKB simulations for the complete vortex flow, as illustrated in figure 9. We consider a thin ray tube which loses its initial circular shape within the vortex velocity field and becomes elliptical. The ratio of the short axis of the elliptical cross-section to the radius of the initial circular cross-section is proportional to δ/L. Therefore, we

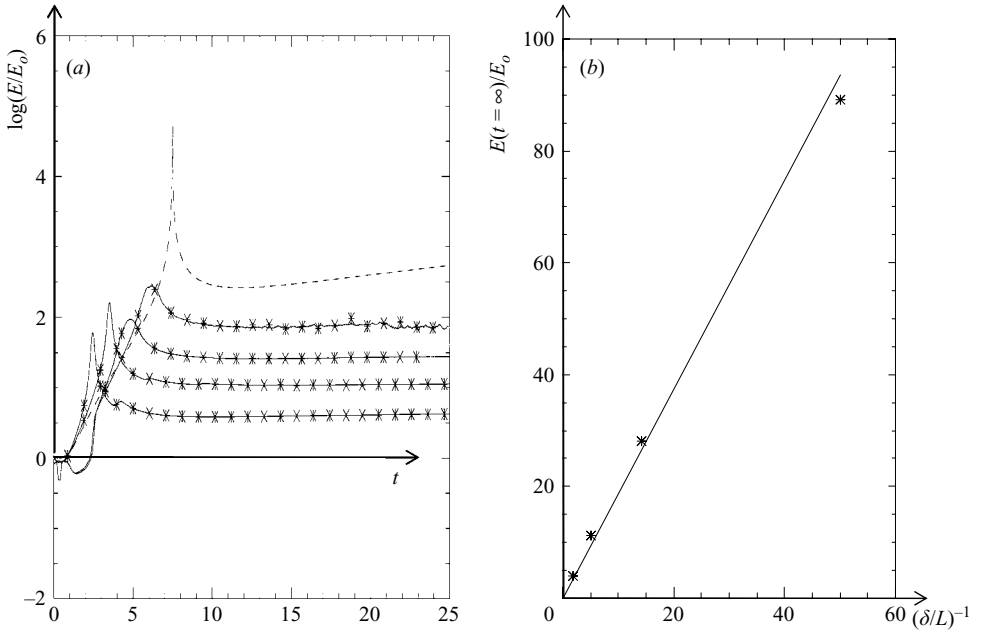

FIGURE 11. (*a*) Evolution of energy (logarithmic scale) along rays propagating in front of a weakly baroclinic flow ($U_L/U_H = 4$), for different values of δ/L. ——, analytical solution for $\delta/L = 0$; – – –, numerical solutions for $\delta/L = 0.54, 0.20, 0.07, 0.02$. (*b*) Final energy amplification as a function of the parameter $(\delta/L)^{-1}$. The stars are numerically calculated points for $\delta/L = 0.54, 0.20, 0.07, 0.02$, and the bold line is the theorical scaling $E/E_o \approx (\delta/L)^{-1}$ (see text).

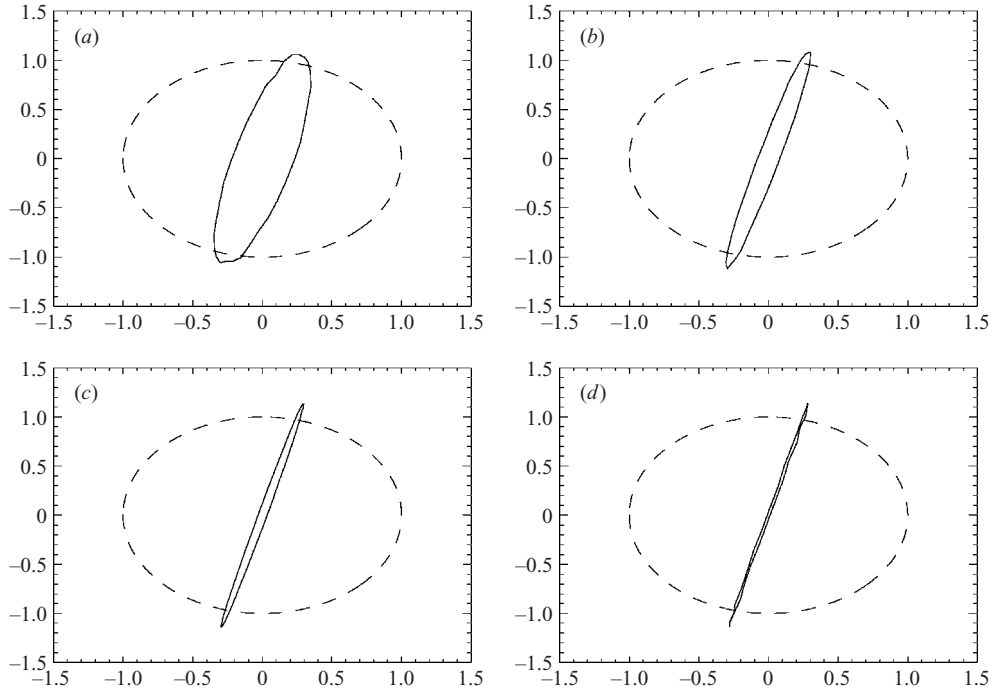

FIGURE 12. Cross-sections of the tube of rays traced in figure 11 at $t = 25$. – – –, initial circular shape; ——, final shape at $t = 25$. Values of δ/L: (*a*) 0.54, (*b*) 0.20, (*c*) 0.07, (*d*) 0.02.

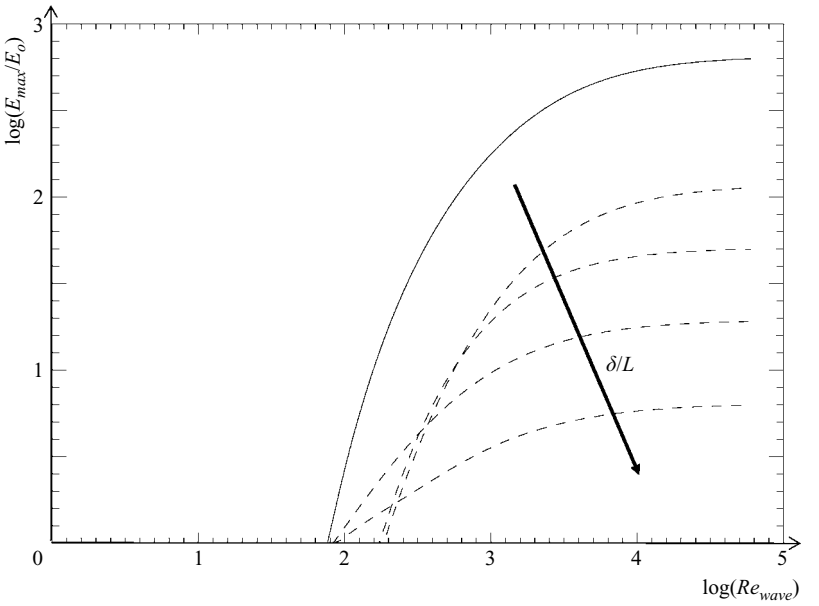

FIGURE 13. Maximum energy amplification as a function of the Re_{wave} (logarithmic scales) for different values of δ/L and rays propagating in front of a weakly baroclinic flow ($U_L/U_H = 4$). ——, prediction for $\delta/L = 0$; – – –, predictions for $\delta/L = 0.54, 0.20, 0.07, 0.02$.

expect a scaling of the final energy amplification with $(\delta/L)^{-1}$. This is confirmed by the numerical results plotted in figure 11(*b*).

Trapped waves still sustain infinite stretching of their wave vector, and because of conservation of the energy density, E, growing amplitudes imply nonlinear effects or wave-breaking. Therefore, flow curvature alone is not sufficient to prevent nonlinear effects or wave-breaking, and will only delay their occurrence, but viscous effects do constrain the wave amplitude (see Booker & Bretherton 1967). The viscous damping rate increases with the decrease in wavelength and may balance the energy amplification associated with the trapping process. For a stratified shear flow without background rotation and waves propagating along the horizontal flow direction (see Booker & Bretherton 1967), the maximum value of the energy amplification becomes a function of the non-dimensional number $U_H/\nu k_y^2$, where U_H is the vertical shear, and k_y is the component of the wave number parallel to the flow. For geostrophic jets studied by Olbers (1980) and Staquet & Huerre (2002), the maximal value of energy amplification depends also on the non-dimensional parameters N_o/f, and width to height ratio L/H. Without aiming at a full description of the dependence of this maximum energy amplification, we can follow Booker & Bretherton (1967) and estimate the relative importance of the trapping effect compared to the viscous damping, using a Reynolds number, Re_{wave}, defined as

$$Re_{wave} = \frac{U_{max}}{\sqrt{(L-R)^2 + H^2}\nu k^2}. \tag{4.4}$$

For high Re_{wave}, the final energy amplification is determined by the curvature parameter δ/L and the amplification will follow the predictions of the inviscid model for a long time. The interaction is expected to give rise to strong nonlinear effects. For low Re_{wave}, the viscous damping will quickly suppress the energy amplification and all the incident wave energy will be dissipated by diffusive processes. In figure 13,

the dependence of the maximum value of the energy amplification is plotted as a function of Re_{wave} for the ray in figure 11. This maximum value is deduced from energy evolution curves of figure 11(*a*), where the reflection peak is replaced by a smooth profile. The solid line corresponds to the zero-curvature limit $\delta/L \to 0$ (or $kFr \to \infty$). A minimal value of Re_{wave} is then required for an amplification to occur. Dashed lines correspond to different values of the curvature δ/L. The minimal value of Re_{wave} that is required for energy amplification to occur, depends weakly on the curvature δ/L since viscous effects act on relatively small scales compared to the curvature. In the limit of high Re_{wave}, the maximum energy amplification decreases with δ/L.

5. Conclusions

We have investigated various interactions of inertia–gravity waves with an isolated Rankine-type vortex. Numerical simulations based upon the WKB equations in cylindrical coordinates have shown a very rich ensemble of possible ray paths interacting with the axisymmetric shear flow of a vortex as is demonstrated by figure 3, with trapping regions depending on kFr, H/R indicated in figures 2, 4 and 8, and trapping efficiency in figure 7. The non-dimensional parameter kFr, which measures the strength of the interaction, can be written as $kFr = Fr(2\pi R/\lambda) = 2\pi U/(N\lambda)$ (with λ the incident wave-length) and represents the ratio between the wave phase-speed and the vortex speed.

For a relatively weak vortex, $Fr(R/\lambda) \ll 1$, rays propagate through the vortex velocity field and are refracted. In this case, the vortex may still experience the recoil force, proposed by Bühler & McIntyre (2003). The impact on the vortex kinematics is beyond the scope of the present paper and will be considered elsewhere.

For a relatively strong vortex, i.e. $Fr(R/\lambda) > 1$, part of the incident wave field is found to decrease in wavelength while its energy is eventually trapped. The localizations of these trapped rays in the vortex field depend on the vortex aspect ratio H/R. The density of the trapped rays in a meridional cross-section increases with FrR/λ, associated with a narrowing of the trapping region. This narrowing is interpreted as a decrease of the curvature parameter δ/L, where δ is the thickness of the wave guide predicted by Olbers (1980) for a unidirectional flow. Finite values of δ/L lead to finite energy amplification in the inviscid approximation, the infinite amplification predicted for unidirectional flows being reached in the limit $\delta/L \to 0$. When viscous effects are taken into account, the efficiency of the energy amplification driven by the trapping process becomes also a function of a wave Reynolds number, Re_{wave}.

For tall vortices with $H/R \gg 1$, the waves propagating against the vortex velocity field are trapped in the periphery of the vortex in a vertical and cylindrically shaped region that is approximately delimited by iso-surfaces of U/r and symmetric with respect to the horizontal mid-plane. In this region, waves exhibit high values of intrinsic frequency ω_o, and breaking may occur through instabilities similar to the wave-breaking in barotropic jets studied by Staquet & Huerre (2002). For flat vortices with $H/R < 1$, waves propagating along the vortex flow are trapped in a region of which the shape is, in approximation, still delimited by iso-surfaces of U/r, but which extends deeply inside the core of the vortex, where U/r is roughly r-independent because of the Gaussian profile in azimuthal velocity z. The symmetry about the mid-plane $z = 0$ is broken and waves propagating downwards (upwards) are trapped in the upper (lower) half-plane. These trapped waves exhibit low values of intrinsic frequency ω_o, and may break through the instability of near-inertia gravity waves.

Finally, we note that the use of the WKB approximation is questionable for rays that cross the middle plane $z = 0$ inside the vortex core, i.e. weakly interacting rays, where

the right-hand side of (2.6)–(2.10) cannot be neglected. There, the vortex velocity field may modify the dispersion relationship and enhance a – with Ro-number increasing – asymmetry in the interaction of waves with anti-cyclonic and cyclonic vortices. This is left open for further work.

The authors gratefully acknowledge financial support from contracts ACI-CATNAT 2001-83 and ACI-PCN-2002 which made this research possible.

Appendix. WKB equations in a cylindrical coordinate system

To solve the ray and refraction equations (2.13) and (2.15) for a vortex flow, it is more convenient to write them in a cylindrical reference frame $(0, \boldsymbol{e}_r, \boldsymbol{e}_\theta, \boldsymbol{e}_z)$. We consider an axisymmetric vortex described by an azimuthal velocity field $U_\theta(r, z)$ and a buoyancy frequency field $N(r, z)$, and components of the wave-vector noted k_r, k_θ, k_z. In the cylindrical reference frame, it is straightforward to show that the set of ray equations (2.13) reads

$$\frac{\mathrm{d}r}{\mathrm{d}t} = v_{gr} = \frac{N^2 - \omega_o^2}{\omega_o k^2} k_r, \quad \frac{\mathrm{d}\theta}{\mathrm{d}t} = \frac{v_{g\theta} + U}{r} = \frac{1}{r}\left(\frac{N^2 - \omega_o^2}{\omega_o k^2} k_\theta + U\right), \quad \text{(A 1), (A 2)}$$

$$\frac{\mathrm{d}z}{\mathrm{d}t} = v_{gz} = -\frac{\omega_0^2 - f^2}{\omega_0 k^2} k_z, \quad \text{(A 3)}$$

where v_{gr}, $v_{g\theta}$ and v_{gz} are the components of the intrinsic group velocity in the cylindrical coordinates system, deduced from formula (2.14), after changing (x, y) into (r, θ).

The refraction equation (2.15) determines the evolution of the wave-vector components along a ray described by (A 1)–(A 3). Since $\boldsymbol{k} = k_r \boldsymbol{e}_r + k_\theta \boldsymbol{e}_\theta + k_z \boldsymbol{e}_z$, $\mathrm{d}\boldsymbol{e}_r/\mathrm{d}t = \mathrm{d}\theta/\mathrm{d}t\, \boldsymbol{e}_\theta$ and $\mathrm{d}\boldsymbol{e}_\theta/\mathrm{d}t = -\mathrm{d}\theta/\mathrm{d}t\, \boldsymbol{e}_r$, the left-hand side of (2.15) reads

$$\frac{\mathrm{d}\boldsymbol{k}}{\mathrm{d}t} = \left(\frac{\mathrm{d}k_r}{\mathrm{d}t} + k_r \frac{\mathrm{d}\theta}{\mathrm{d}t}\right) \boldsymbol{e}_r + \left(\frac{\mathrm{d}k_\theta}{\mathrm{d}t} - k_\theta \frac{\mathrm{d}\theta}{\mathrm{d}t}\right) \boldsymbol{e}_\theta + \left(\frac{\mathrm{d}k_z}{\mathrm{d}t}\right) \boldsymbol{e}_z. \quad \text{(A 4)}$$

The first term on the right-hand side is a gradient operator, easily transformed into a cylindrical coordinate system. The second term on the right-hand side is an operator that will be denoted $\boldsymbol{\Gamma}$,

$$\boldsymbol{\Gamma} = \left(-k_x \frac{\partial U_x}{\partial x} - k_y \frac{\partial U_y}{\partial x}\right) \boldsymbol{e}_x + \left(-k_x \frac{\partial U_x}{\partial y} - k_y \frac{\partial U_y}{\partial y}\right) \boldsymbol{e}_y + \left(-k_x \frac{\partial U_x}{\partial z} - k_y \frac{\partial U_y}{\partial z}\right) \boldsymbol{e}_z, \quad \text{(A 5)}$$

where U_x and U_y are the Cartesian components of the azimuthal velocity field U_θ. Partial derivatives of these Cartesian components can be expressed as linear combinations of the partial derivatives of the azimuthal velocity field, $\partial U_\theta/\partial r$ and $\partial U_\theta/\partial z$. Also $\boldsymbol{e}_x$ and $\boldsymbol{e}_y$ are easily transformed into $\boldsymbol{e}_r$ and $\boldsymbol{e}_\theta$, so that in cylindrical coordinates Γ reads

$$\boldsymbol{\Gamma} = \left(-k_\theta \frac{\partial U}{\partial r}\right) \boldsymbol{e}_r + \left(-k_r \frac{U}{r}\right) \boldsymbol{e}_\theta + \left(-k_\theta \frac{\partial U}{\partial z}\right) \boldsymbol{e}_z. \quad \text{(A 6)}$$

Using (A 4) and (A 6), the projection of the refraction equation (2.15) on the different components of the cylindrical coordinate system yields

$$\frac{\mathrm{d}k_r}{\mathrm{d}t} = +k_\theta \frac{v_{g\theta} + U}{r} - \frac{N}{\omega_0}\left(\frac{\omega_0^2 - f^2}{N^2 - f^2}\right) \frac{\partial N}{\partial r} - k_\theta \frac{\partial U}{\partial r}, \quad \text{(A 7)}$$

$$\frac{\mathrm{d}k_\theta}{\mathrm{d}t} = -k_r \frac{v_{g\theta}}{r}, \quad \frac{\mathrm{d}k_z}{\mathrm{d}t} = -\frac{N}{\omega_0}\left(\frac{\omega_0^2 - f^2}{N^2 - f^2}\right) \frac{\partial N}{\partial z} - k_\theta \frac{\partial U}{\partial z}. \quad \text{(A 8), (A 9)}$$

Note in (A 1)–(A 2) that $v_{gr}/v_{g\theta} = k_r/k_\theta$, so that equation (A 8) becomes $\mathrm{d}\ln(rk_\theta)/\mathrm{d}t = 0$, leading to conservation of rk_θ along a ray. Therefore, the system of six equations (A 1)–(A 3) and (A 7)–(A 9) can be solved by considering only five components.

REFERENCES

Acheson, D. J. 1976 On over-reflexion. *J. Fluid. Mech.* **77**, 433–472.

Badulin, S. I. & Shrira, V. I. 1993 On the irreversibility of internal-wave dynamics due to wave trapping by mean flow inhomogeneities. Part 1. Local analysis. *J. Fluid Mech.* **251**, 21–53.

Badulin, S. I., Shrira, V. I. & Tsimring, L. Sh. 1984 The trapping and vertical focusing of internal waves in a pycnocline due to the horizontal inhomogeneities of density and currents. *J. Fluid. Mech.* **158**, 199–218.

Bretherton, F. P. 1966 The propagation of groups of internal gravity waves in a shear flow. *Q. J. R. Met. Soc.* **92**, 466–480.

Booker, J. R. & Bretherton, F. P. 1967 The critical layer for internal gravity waves in a shear flow. *J. Fluid Mech.* **27**, 513–539.

Bühler, O. & McIntyre, M. 2003 Remote recoil : a new wave–mean flow interaction effect. *J. Fluid Mech.* **492**, 207–230.

Dörnbrack, A. 1998 Turbulent mixing by breaking gravity waves. *J. Fluid Mech.* **375**, 113–141.

van Duin, C. A. & Kelder, H. 1998 Reflection properties of internal gravity waves incident upon a hyperbolic tangent shear layer. *J. Fluid Mech.* **120**, 505–521.

Edwards, N. R. & Staquet, C. 2005 Focusing of an inertia–gravity wave packet by a baroclinic shear flow. *Dyn. Atmos. Oceans* **40**, 91–113.

Flierl, G. R. 1988 On the instability of geostrophic vortices. *J. Fluid Mech.* **197**, 349–388.

Flór, J. B., Fernando, H. J. S. & Van Heijst, G. J. F. 1994 The evolution of an isolated turbulent region in a two-layer fluid. *Phys. Fluids* **6**, 287–296.

Galmiche, M., Thual, O. & Bonneton, P. 2000 Wave/wave interaction producing horizontal mean flows in stably stratified fluids. *Dyn. Atmos. Oceans* **31**, 193–207.

Ivanov, Y. A. & Morozov, Ye. G. 1974 Deformation of internal gravity waves by a stream with horizontal shear. *Oceanology* **14**, 376–380.

Jones, W. L. 1968 Reflexion and stability of waves in stably stratified fluids with shear flow: a numerical study. *J. Fluid Mech.* **34**, 609–624.

Koop, C. G. 1981 A preliminary investigation of internal gravity waves with a steady shearing motion. *J. Fluid Mech.* **113**, 347–386.

Leblond, P. H. & Mysak, L. A. 1978 *Waves in the Ocean.* Elsevier Oceanography Series 20, 601pp.

Lelong, M. P. & Riley, J. J. 1991 Internal wave-vortical mode interactions in strongly stratified flows. *J. Fluid Mech.* **232**, 1–19.

Lighthill, J. 1978 *Waves in Fluids.* Cambridge University Press.

Lighthill, J. 1996 Internal waves and related initial-value problems. *Dyn. Atmos. Oceans* **23**, 3–17.

Moulin, F. & Flór, J.-B. 2005 Experimental study on the wave-breaking and mixing properties of a tall vortex. *Dyn. Atm. Oceans* **40**, 115–130.

Olbers, Dirk, J. 1980 The propagation of internal waves in a geostrophic current. *J. Phys. Oceanogr.* **11**, 1224–1233.

Öllers, M. 2003 Influence of inertia–gravity waves on the permeability of the Antarctic polar vortex edge, pp. 1–139. Library Technische Universiteit Eindhoven.

Staquet, C. & Huerre, G. 2002 On transport across a barotropic shear flow by breaking inertia–gravity waves. *Phys. Fluids* **14**, 1993–2006.

Staquet, C. & Sommeria, J. 2002 Internal gravity waves, from instabilities to turbulence. *Annu. Rev. Fluid Mech.* **34**, 559–593.

Turner, J. S. 1973 *Buoyancy Effects in Fluids.* Cambridge University Press.